Microsc. Microanal. 6, 343–352, 2000
DOI: 10.1007/s100050010045

Microscopy AND Microanalysis

Z-contrast Imaging in an Aberration-corrected Scanning Transmission Electron Microscope

S.J. Pennycook,[1]* B. Rafferty,[1,2] and P.D. Nellist[3]

[1]*Solid State Division, Oak Ridge National Laboratory, P.O. Box 2008, Oak Ridge, TN 37831-6030*
[2]*Cavendish Laboratory, Madingley Road, Cambridge CB3 0HE, UK*
[3]*Nanoscale Physics Research Laboratory, School of Physics and Astronomy, The University of Birmingham, Birmingham, B15 2TT, UK*

Abstract: We show that in the limit of a large objective (probe-forming) aperture, relevant to a spherical aberration corrected microscope, the Z-contrast image of a zone-axis crystal becomes an image of the 1s Bloch states. The limiting resolution is therefore the width of the Bloch states, which may be greater than that of the free probe. Nevertheless, enormous gains in image quality are expected from the improved contrast and signal-to-noise ratio. We present an analytical channeling model for the thickness dependence of the Z-contrast image in a zone-axis crystal, and show that, at large thicknesses, columnar intensities become proportional to the mean square atomic number, Z^2.

Key words: scanning transmission electron microscopy, aberration correction, Z-contrast, high angle annular dark field, channeling, Bloch states

Introduction

The recent demonstration of spherical aberration correction for both the transmission and scanning transmission electron microscopes promises to revolutionize the field of microscopy and microanalysis (Haider et al., 1998; Krivanek et al., 1999). Here we argue that the potential benefits for the scanning transmission electron microscope (STEM) far exceed those for the conventional transmission electron microscope (CTEM). Some of these benefits are intrinsic to incoherent imaging: the potential factor of two improvement in image resolution and the lack of interference artifacts were first pointed out by Lord Rayleigh in the context of light microscopy (Rayleigh, 1896). These advantages will still apply after aberration correction. In a zone-axis crystal, the incoherent mode shows no contrast oscillations with objective lens defocus or specimen thickness. Such effects will remain in the aberration-corrected TEM, as the image contrast relies on the coherent interference of Bragg beams in the image plane. This is just a manifestation of the well known phase problem inherent to phase-contrast microscopy. There is no phase problem in an incoherent image, because there are no phases. The image is given by a simple convolution between an object function representing the scattering power of the specimen and a resolution function, the probe intensity profile,

$$I(\mathbf{R}) = O(\mathbf{R}) * P^2(\mathbf{R}). \quad (1)$$

Intensity maxima in an incoherent image correlate closely with peaks in the object function and, because the only unknown quantity is the object function, which is real and positive, the image can be directly inverted.

Received December 8, 1999; accepted January 3, 2000.
*Corresponding author

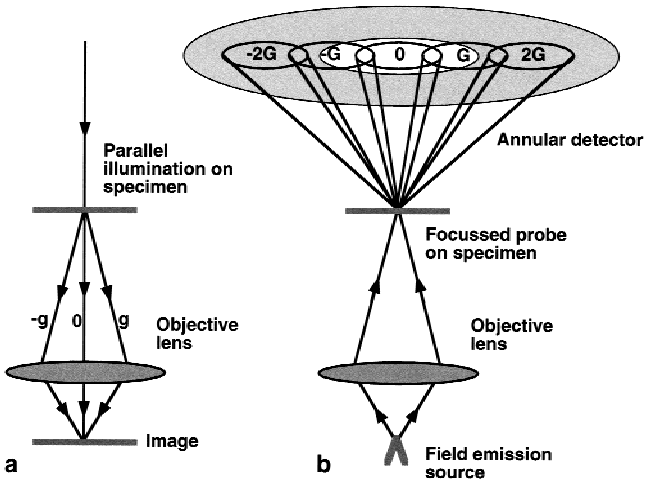

Figure 1. Diagram showing the beams interfering to form the image contrast in (**a**) axial phase contrast imaging in transmission electron microscopy (TEM), and (**b**) annular dark field imaging in scanning transmission electron microscopy (STEM). In the TEM, contrast comes predominantly from interference between the zero order beam and the diffracted beams ±**g.** In the STEM, image contrast comes from the overlapping regions of the convergent beam discs and, near the limit of resolution, involves interference between beams close to +**g** and −**g** in the two discs. Note that the STEM specimen is shown with half the spacing of the TEM specimen, i.e., the diffraction vector **G** = 2**g.** This is the origin of the double resolution in STEM.

The recent demonstration of sub-Ångstrom information transfer in an incoherent image (Nellist and Pennycook, 1998a) well demonstrates the intrinsic resolution advantage of the incoherent mode, but also highlights another crucial advantage. The incoherent mode is very much less sensitive to instabilities than the coherent mode. Contrast transfer is not reduced by an exponential damping function, as is the phase contrast transfer function; the information limit where this function reaches zero is not the information limit of the microscope as commonly supposed, just the information limit of the phase contrast mode. In the incoherent case, contrast arises from the overlap of convergent beam diffraction discs on the annular detector (Spence and Cowley, 1978). As the resolution increases, the regions of overlap become narrower and the interfering beams travel almost equal optical path lengths either side of the optical axis, as shown in Figure 1. Such beams are therefore almost insensitive to changes in optical path lengths introduced through instabilities such as fluctuations in objective lens current or high voltage supply. The phase contrast mode involves interference between the zero order beam and diffracted beams at the edge of the aperture, which traverse very different optical paths and are therefore much more sensitive to chromatic aberration effects.

Another very important advantage of the aberration corrected (STEM) is that it automatically allows atomic column resolved analysis simply by stopping the probe on a particular column selected from the image. Electron energy loss spectroscopy (EELS) can then be performed on individual columns (Browning et al., 1993; Batson, 1993; Duscher et al., 1998; Muller, 1999), and the greatly reduced overlap of the probe with neighboring columns will give much greater sensitivity. Indeed, detection of single impurity atoms seems a likely possibility. In this context, it is worth remembering that the more focused probe will cause increased knock-on damage events, but may not result in a large increase in ionization damage because inelastic valence excitations are much less localized and therefore insensitive to the improved focusing of the probe.

Below we examine the theory of STEM imaging paying particular attention to the effect of increasing the size of the objective aperture, and present some exciting simulated images.

Diffraction Channeling

The fact that diffraction and channeling represent simply reciprocal space and real space viewpoints of the same physical phenomenon was first pointed out explicitly by Howie (1967). It provided the basis for a physical understanding of all localized scattering processes in electron microscopy; an early success was the explanation of anomalous absorption as the increased localization of the electron flux at the atom sites at incident beam directions near a crystal plane or zone axis direction, leading to increased high angle diffuse scattering (Howie and Whelan, 1961; Heidenreich, 1962; Hirsch et al., 1965). It later explained the increased X-ray emission found under such conditions (Hirsch et al., 1962; Cherns et al., 1987), which now forms the basis for electron channeling analysis (Spence and Tafto, 1983; Pennycook and Narayan, 1985). Contrast from other secondary excitations such as cathodoluminescence could also be explained quantitatively (Pennycook and Howie, 1980), and it provided the first explanation for the incoherent nature of the Z-contrast image, regarding the image as being created by incoherent large angle electron scattering events (Pennycook and Jesson, 1990, 1991, 1992).

Subsequent detailed investigation showed that the detector geometry was sufficient to destroy coherence in the

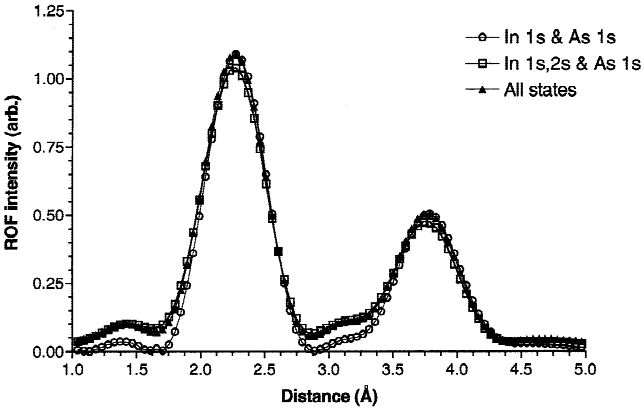

Figure 2. Residual object function (ROF) profile along ⟨001⟩ through the center of the dumbbell for InAs ⟨110⟩ showing the dominant contribution of the 1s states. The calculation is for 300 kV electrons using 411 beams and a detector inner angle of 60 mrad.

Table 1. Peak Intensities of the Residual Object Function in InAs and GaAs ⟨110⟩ for Various Combinations of Bloch States Showing the Dominance of the 1s States[a]

		Residual object function (ROF)		
III/V	State (s)	III site	V site	*n*
InAs	In 1s; As 1s	1.08	0.504	1.93
	In 1s, 2s; As 1s	1.04	0.476	1.97
	All	1.09	0.508	1.93
GaAs	Ga 1s; As 1s	0.441	0.504	2.13
	Ga 1s, 2s; As 1s, 2s	0.430	0.490	2.1
	All	0.4297	0.4928	2.19

[a]Also shown is the exponent *n* of the intensity ratio expressed as Z^n. Calculations assume 300 kV electrons, a 60 mrad inner detector angle, and include 411 beams for InAs and 333 beams for GaAs.

transverse plane (Jesson and Pennycook, 1993), creating *intercolumn* incoherence between neighboring atomic columns, and an image formed from purely coherent scattering would show incoherent characteristics. Coherent characteristics would reveal themselves in the thickness dependence of the image intensity, however, which would show strong thickness fringes. Thermal vibrations were shown to be effective in breaking the coherence along a column (Jesson and Pennycook, 1995), leading the *intracolumn* incoherence, which largely removed the thickness oscillations in agreement with experimental observations. Experiment and theory, both Bloch wave (Pennycook and Jesson, 1990) and multislice calculations (Loane et al., 1992; Anderson et al., 1997; Hartel et al., 1996), were largely in agreement. Here we present the reciprocal space Bloch wave formulation introduced by Nellist and Pennycook (1998b).

Direct Imaging of 1s Bloch States

To achieve an electron optically limited probe, we assume an infinite demagnification of the source so that a plane wave is incident on the objective aperture. The probe profile is then just the intensity distribution in the object plane, the square of the Airy disc amplitude distribution. Denoting transverse coordinates by upper case letters, and the beam direction as z, positions in the objective back focal plane are labeled by the two-dimensional vector **K** and positions in real space by (**R**,z). The objective lens transfer function due to spherical aberration and defocus, is given by

$$A(\mathbf{K}) = H(\mathbf{K})\, e^{i\gamma(K)} \tag{2}$$

where H(**K**) is the aperture function, unity inside the aperture and zero elsewhere, $|K| = \chi\theta$ is the transverse component of the incident electron wavevector $\chi = 2\pi/\lambda$, θ is the angle to the objective axis, and λ is the electron wavelength. In an uncorrected microscope, the transfer function phase factor γ is dominated by the defocus Δf and the third order objective lens spherical aberration coefficient C_s,

$$\gamma = \frac{1}{2\chi}\left(\Delta f K^2 + \frac{1}{2} C_s \frac{K^4}{\chi^2}\right). \tag{3}$$

The amplitude distribution $P(\mathbf{R} - \mathbf{R}_0)$ of the STEM probe at location $\mathbf{R}_0$ is obtained by integrating the transfer function over the objective aperture,

$$P(\mathbf{R} - \mathbf{R}_0) = \int A(\mathbf{K})\, e^{i\mathbf{K}\cdot(\mathbf{R}-\mathbf{R}_0)}\, d\mathbf{K}. \tag{4}$$

The probe intensity distribution in free space is given by $P^2(\mathbf{R})$. Inside a zone-axis crystal, each incident plane wave $e^{i\,\mathbf{K}\cdot\mathbf{R}}$ must be replaced by a set of two-dimensional Bloch states $b^j(\mathbf{K},\mathbf{R})$ with excitation coefficients $\varepsilon^j(\mathbf{K})$ and absorption coefficients $\mu^j(\mathbf{K})$ propagating along the z-axis with wavevector $k_z^j(\mathbf{K})$. The probe amplitude at depth z in the crystal becomes

$$P(\mathbf{R} - \mathbf{R}_0, z) = \int A(\mathbf{K}) \sum_j \varepsilon^j(\mathbf{K}) b^j(\mathbf{K},\mathbf{R}) e^{i\mathbf{K}\cdot(\mathbf{R}-\mathbf{R}_0)} e^{-ik_z^j(\mathbf{K})z} e^{-\mu^j(\mathbf{K})z} d\mathbf{K} \tag{5}$$

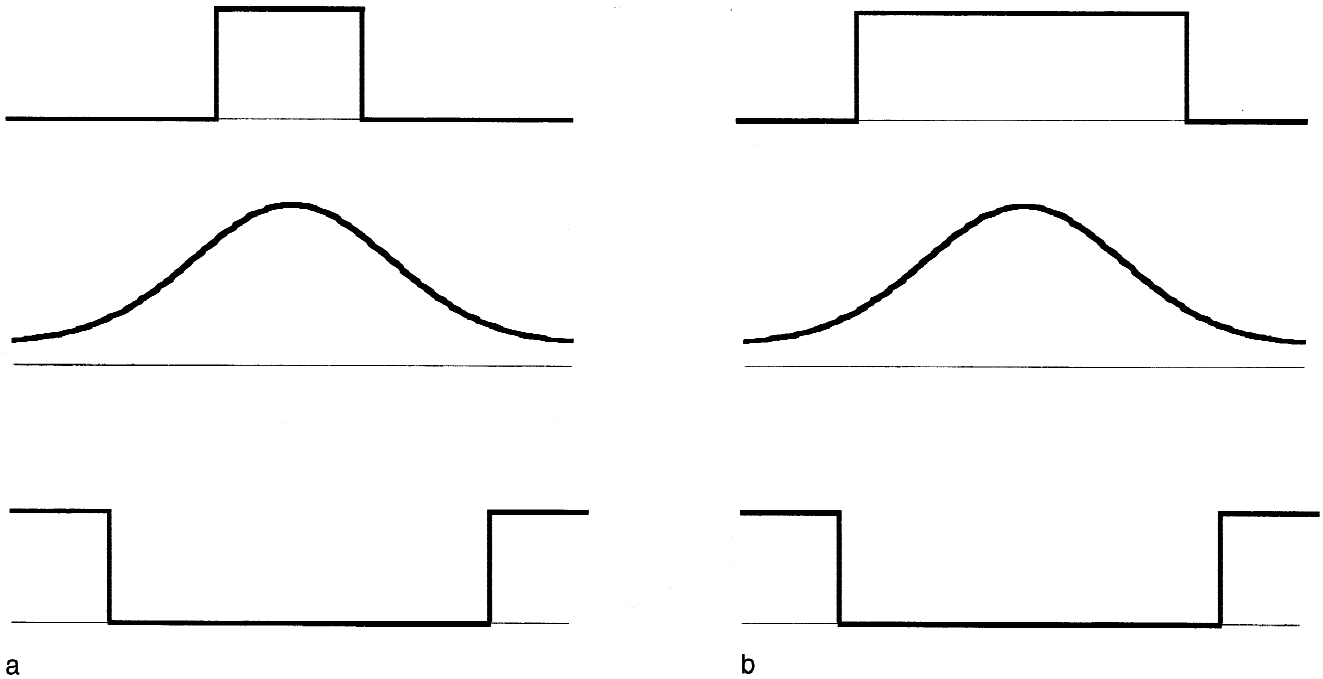

Figure 3. Schematic representation of the aperture function H(**K**) (**top**), the 1s Bloch state excitation ε(**K**) (**middle**), and the detector function D(**K**) (**bottom**) for (**a**) today's objective aperture and (**b**) the larger objective aperture of an aberration-corrected STEM.

and the probe intensity inside the crystal is now given by $P^2(\mathbf{R} - \mathbf{R}_0, z)$. As shown by Nellist and Pennycook (1998a), this can be Fourier transformed with respect to $\mathbf{R}_0$ to give the intensity distribution in reciprocal space, and then integrated over the annular detector $D(\mathbf{K}_f)$ to give the ρ spatial frequency component of the image intensity,

$$I(\rho,z) = \int D(\mathbf{K}_f) d\mathbf{K}_f \int A(\mathbf{K}) A^*(\mathbf{K}+\rho) \sum_{j,k} \varepsilon^j(\mathbf{K}) \varepsilon^{k*}(\mathbf{K}+\rho) b_{\mathbf{K}_f}{}^j(\mathbf{K}) b_{\mathbf{K}_f}{}^{k*}(\mathbf{K}) \times e^{-i[k_z{}^j(\mathbf{K}) - k_z{}^k(\mathbf{K})]z} e^{-[\mu^j(\mathbf{K}) + \mu^k(\mathbf{K})]z} d\mathbf{K}, \quad (6)$$

where $b_{\mathbf{K}_f}{}^j(\mathbf{K})$ represents the $\mathbf{K}_f$ Fourier component of the Bloch state j and * denotes complex conjugate. It is easy to see that strong contributions to the intensity can only come from those Bloch states that contain frequency components $b_{\mathbf{K}_f}$ that extend over the detector. For a high angle detector, this implies that only states that are very broad in reciprocal space will contribute, states that are sharply peaked in real space. The detector therefore preferentially selects the 1s states. The advantage of this reciprocal space formulation is that the contributions of different Bloch states can be determined directly by performing the detector sum,

$$C_{jk} = \int D(\mathbf{K}_f)\, b_{\mathbf{K}_f}{}^j\, b_{\mathbf{K}_f}{}^{k*}\, d\mathbf{K}_f. \quad (7)$$

This reciprocal space representation allows the important Bloch state contributions to the image intensity to be immediately identified. It gives vast savings in computer time compared to multislice approaches, where all the beams reaching the detector are calculated even if they eventually sum to zero. Selecting specific j,k Bloch state combinations in Eq. (6) and transforming back to real space, the contribution of different states to the image intensity can be readily calculated. In the high thickness limit, only the terms j = k survive because of the exponential damping factor, which we refer to as the residual object function, ROF. Figure 2 shows a plot of the ROF for InAs $\langle 110 \rangle$ at $\mathbf{K} = 0$. Even for the heavy In column, the 1s state is found to contribute 99.5% of the image contrast. Including all other Bloch states just puts a small background intensity onto the image. Particularly interesting is the behavior of the 2s state on the In column. Despite the fact that its excitation $\varepsilon^{2s} = 0.90$ is much higher than that of the 1s state, $\varepsilon^{1s} = 0.24$, it gives negligible contribution to the image contrast. This highlights the strong 1s filtering effect of the high angle detector. Table 1 shows values of the ROF in

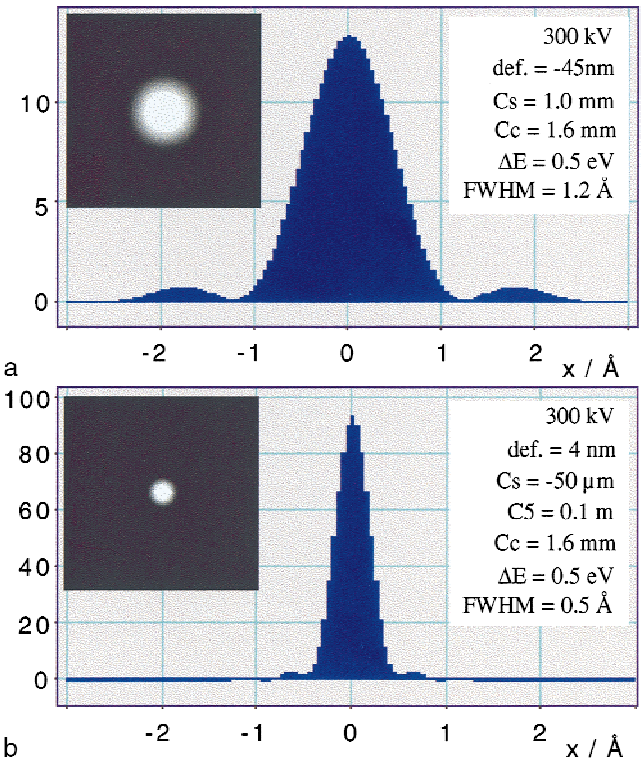

Figure 4. Theoretical probe profiles for the VG Microscopes HB603U STEM at Oak Ridge National Laboratory. **a:** Today's probe with a 1.3 Å full-width-half maximum (FWHM); **b:** expected probe after correction of third order spherical aberration, showing approximately a sixfold increase in peak intensity accompanied by a decrease in FWHM to 0.5 Å and a reduction in probe tails.

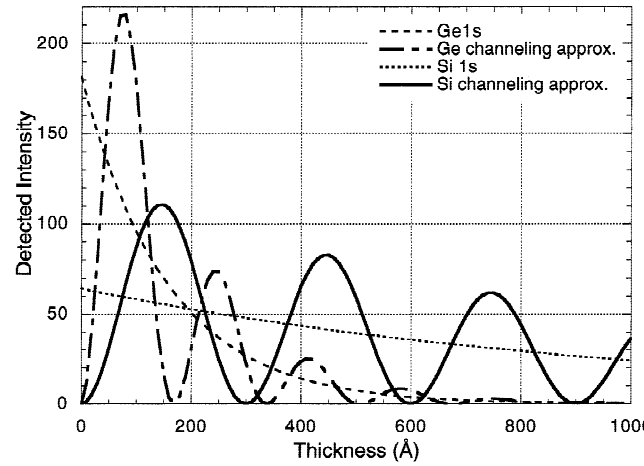

Figure 5. Intensity of coherent diffracted beams falling on the high angle annular detector from Si and Ge ⟨110⟩ for the 1s states alone, Eq. (12), and the channeling approximation, Eq. (16). Parameters are: Si, ξ = 300 Å; μ^{1s} = 0.0048; Ge, ξ = 169 Å; μ^{1s} = 0.0032.

InAs and GaAs for various combinations of 1s and 2s states compared to all states. We also give the Z-dependence of the peak intensity of the ROF, which is seen to closely approximate the Z^2 dependence expected for unscreened Rutherford scattering.

The dominance of the 1s states arises because they are so sharply peaked in real space. For typical intercolumn spacings, they are essentially independent of neighboring atomic columns; they do not overlap, and hence are nondispersive in reciprocal space. This means that the same dominance of 1s states is found for other incident beam directions within the objective aperture. Thus, the entire image intensity is dominated by 1s states, and Eq. (6) can be approximated by

$$I(\rho,z) = C_{1s}\, e^{-2\mu^{1s}z} \int A(\mathbf{K})A^*(\mathbf{K}+\rho)\, \varepsilon^{1s}(\mathbf{K})\varepsilon^{1s*}(\mathbf{K}+\rho)\, d\mathbf{K}, \tag{8}$$

where C_{1s} is the sum of the 1s state components over the detector

$$C_{1s} = \int D(\mathbf{K}_f)\, b_{\mathbf{K}_f}{}^{1s}\, b_{\mathbf{K}_f}{}^{1s*}\, d\mathbf{K}_f. \tag{9}$$

If it were not for the presence of the ε^{1s} terms in Eq. (8), we would just have the autocorrelation function of the objective lens transfer function weighted by C_{1s} and the 1s state absorption. Because the Fourier transform of the autocorrelation function is just the free space probe intensity profile, we would have perfect incoherent imaging,

$$I(\mathbf{R}-\mathbf{R}_0,z) = O(\mathbf{R},z) * P^2(\mathbf{R}-\mathbf{R}_0), \tag{10}$$

with an object function

$$O(\mathbf{R},z) = C_{1s}\, e^{-2\mu^{1s}z}\, \delta(\mathbf{R}-\mathbf{R}_i), \tag{11}$$

an array of delta functions at the atomic column positions $\mathbf{R}_i$ weighted by their high angle scattering power.

Because currently available probes are much broader than the 1s states, the 1s state excitation is slowly varying over the objective aperture, and acts as a damping factor. We define an effective probe amplitude inside the crystal as

$$P^{eff}(\mathbf{R}-\mathbf{R}_0) = \int A(\mathbf{K})\, \varepsilon^{1s}(\mathbf{K})\, e^{i\mathbf{K}\cdot(\mathbf{R}-\mathbf{R}_0)}\, d\mathbf{K}, \tag{12}$$

which is slightly broader than the free space probe due to the reduction in 1s state excitation at the edge of the objective aperture (see Fig. 3). In fact, multiplication of the transfer function in reciprocal space by $\varepsilon^{1s}(\mathbf{K})$ is equivalent to a convolution in real space of the probe amplitude profile with the Fourier transfer of the 1s state excitation, which is the 1s Bloch state itself,

$$P^{eff}(\mathbf{R} - \mathbf{R}_0) = P(\mathbf{R} - \mathbf{R}_0) * b^{1s}(\mathbf{R}). \tag{13}$$

It is a minor effect with today's probes, which are large compared to the sub-Ångstrom dimensions of the 1s states, resulting in a few tenths of an Ångstrom broadening and a slight reduction in image contrast.

However, let us now consider what happens if the objective aperture is opened up, as becomes possible with a corrected microscope. It is important to remember that the Bloch state amplitudes are periodic:

$$b_{\mathbf{K}_i}{}^{j}(\mathbf{K}) = b_{\mathbf{K}_{i-\mathbf{g}}}{}^{j}(\mathbf{K} + \mathbf{g}) \tag{14}$$

where $\mathbf{g}$ is a reciprocal lattice vector. But today's objective aperture angles are already comparable to typical crystal $\mathbf{g}$ vectors. If the 1s state amplitudes are constant over today's objective apertures, they will also be constant over the larger apertures of tomorrow. The difference is that the excitation will fall further at the edge of the aperture, as shown in Figure 3. Incident beam components near the periphery of the large objective aperture will be at such a large angle to the objective axis that they will be unlikely to undergo diffraction at all, passing therefore straight through the sample and through the hole in the detector. Therefore, we should be able to open up the objective aperture to close to the inner angle of the detector, and the image resolution will improve, until it is no longer limited by the size of the probe but by the size of the 1s Bloch states. In this limit, we will have a direct image of the 1s Bloch states themselves.

With a large probe, a narrow detector function is required to separate the integration in Eq. (6) into a convolution, but now the probe itself does the job, and we no longer need the detector inner angle to be much higher than the objective aperture radius. It is quite clear that, in the limit of a delta function probe, we obtain a direct image of the 1s Bloch states.

By keeping the same annular detector angles as today, the peak detected intensity will increase. Let us assume that, if we open up the objective aperture by a factor of three, we will need to increase the demagnification by the same factor to avoid being limited by the finite source size, then we have the same total incident current as today. However, as shown in Figure 4, the peak intensity for the VG Microscopes (East Grinstead, UK) HB603 is predicted to increase by a factor of approximately six, due to the reduction in full-width-half-maximum (FWHM) from today's 1.2 Å to a predicted 0.5 Å after correction of third order spherical aberration. Peak image intensities will therefore increase by a factor of 6, signal-to-noise ratio will improve, and, at the same time, the image contrast will increase dramatically.

Channeling Model for the Thickness-dependent Object Function

We have shown that the 1s states are by far the most important single state for scattering to the high angle detector. Nevertheless, not all of the incident beam can be coupled into the 1s states. Because the Bloch states are normalized and form a complete set, if we have a sharply peaked 1s state $b^{1s}(\mathbf{R})$ at a particular atomic column, then the sum of all the other states must be of the form $1 - b^{1s}(\mathbf{R})$ in a thin crystal, which shows an equally sharp dip at the atomic sites. Depth-dependent oscillations come from the beating of these two components. The 1s states are located over the deepest part of the projected potential and so have the highest kinetic energy and the largest $k_z{}^j$. All the other less localized states have very similar $k_z{}^j$ values, and so in thin crystals they all propagate approximately in phase through the thickness z. Therefore it is a good approximation to consider just two components to the electron wave function, the 1s state propagating with wavevector $k_z{}^{1s}$, and a term $1 - b^{1s}(\mathbf{R})$ propagating at an average $k_z{}^0$. The beating between these two components occurs with an extinction distance $\xi = 2\pi/(k_z{}^{1s} - k_z{}^0)$. Channeling models of this sort have proved useful not only for Z-contrast imaging (Pennycook and Jesson, 1992) but also for phase contrast imaging (Van Dyck, 1989; Sinkler and Marks, 1999).

Replacing the C_{1s} term by Z^2, the depth-dependent object function for a column is now given by

$$O(\mathbf{R},z) = Z^2\,[1 - \cos(2\pi z/\xi)]\,e^{-2\mu^{1s}z}. \tag{15}$$

Figure 5 shows a plot of this function for Si and Ge in the ⟨110⟩ orientation, compared to Eq. (11) for the 1s state intensities alone. The decaying thickness fringes reflect the shorter extinction distance and higher absorption for the heavier Ge column, and the saturation value of Z^2 is reached at a lower thickness than in the case of Si.

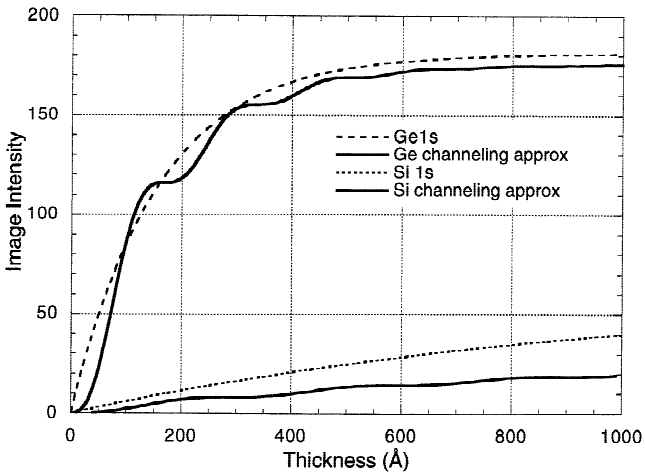

Figure 6. Intensity of incoherent scattering reaching the annular detector from Si and Ge ⟨110⟩ using the channeling approximation, Eq. (16). Parameters are the same as in Figure 5.

So far, although we have included absorption through the exponential decay of the Bloch states, the absorbed electrons have just been removed from the propagating coherent wavefield. In reality, we choose high detector angles so that diffuse scattering dominates the detected intensity and coherence is broken through the thickness of the crystal. If we assume that *all* the high angle beams reaching the detector suffer diffuse scattering, the total detected signal will be the integral of Eq. (15) over the crystal thickness t, giving an object function

$$O_{TDS}(\mathbf{R},t) = \frac{Z^2}{(\xi^2\mu^{1s^2} + \pi^2)}\left[\pi^2(1 - e^{-2\mu^{1s}t}) - \xi^2\mu^{1s^2}e^{-2\mu^{1s}t}\left(1 - \cos\frac{2\pi t}{\xi}\right) - \pi\xi\mu^{1s}e^{-2\mu^{1s}t}\sin\frac{2\pi t}{\xi}\right] \quad (16)$$

which is plotted in Figure 6. The thickness integration has removed the strong dynamical oscillations giving the monotonically increasing intensity similar to that found experimentally. For lower detection angles, a fraction of the coherent high angle beams given by Eq. (15) must be added, and the image contrast begins to show more oscillatory dependence on thickness. At still lower angles, other Bloch states begin to become more important and the incoherent characteristics are progressively lost.

It is important to remember that this channeling theory assumes straight columns with equal scattered intensity from each layer. If this is not the case, the contrast may be more complicated to interpret. For example, a single heavy impurity atom in a light matrix might scatter sufficiently to dominate the image intensity. Its scattered intensity comes from a specific depth in the crystal, and so its contrast is depth-dependent. It will sample the oscillating wavefield of Figure 5, and will show maximum contrast at a depth corresponding to the first channeling peak (Loane et al., 1988; Nakamura et al., 1997; Mitsuishi et al., 1999). Another case concerns local strain fields. If strains are incoherent on the scale of the extinction distance, such as with impurity atoms, then quantitative information can be extracted on the mean square displacements (Hall et al., 1966; Duscher et al., 1998). However, if the strain field is coherent over significant distances, then diffraction contrast will be seen (Perovic et al., 1993), which can be calculated for an incoherent image just as it can for a coherent image, but the intensities are no longer dependent only on Z.

Simulated Images for an Aberration-corrected STEM

Figure 7a shows an image of a 36° [100] symmetric tilt grain boundary in $SrTiO_3$ obtained on the VG Microscopes HB603U STEM at Oak Ridge National Laboratory (Duscher et al., 1998). With an accelerating voltage of 300 kV and an objective lens third order spherical aberration coefficient of 1 mm, the theoretical optimum probe at a Scherzer (1949) (incoherent) defocus has a full width half maximum of 1.3 Å. The Sr and Ti columns are clearly distinguishable from their Z-contrast, and even in the grain boundary core, although the intensities are different from the bulk, the atomic column locations can be seen. Both the Sr and Ti dislocation cores comprising the boundary are seen to contain closely spaced pairs of columns, which presumably are alternately occupied along the tilt axis. This doubled periodicity represents a grain boundary reconstruction analogous to a surface reconstruction. However, the oxygen sites are not visible above the background intensity between the heavy columns. This background is due to the annular shaped probe tail around the central peak (see Fig. 4). In contrast, for the aberration corrected microscope, a 0.5 Å probe is predicted, with much more localized probe tails. Figure 7b is the simulated image for the same boundary, assuming a Z^2 object function, which now has essentially no background between the heavy columns so that the oxygen columns are detectable. The simulation is obtained by convoluting the free space probe with a 1s Bloch state of width 0.8 Å. Noise level is assessed by simulating the image for

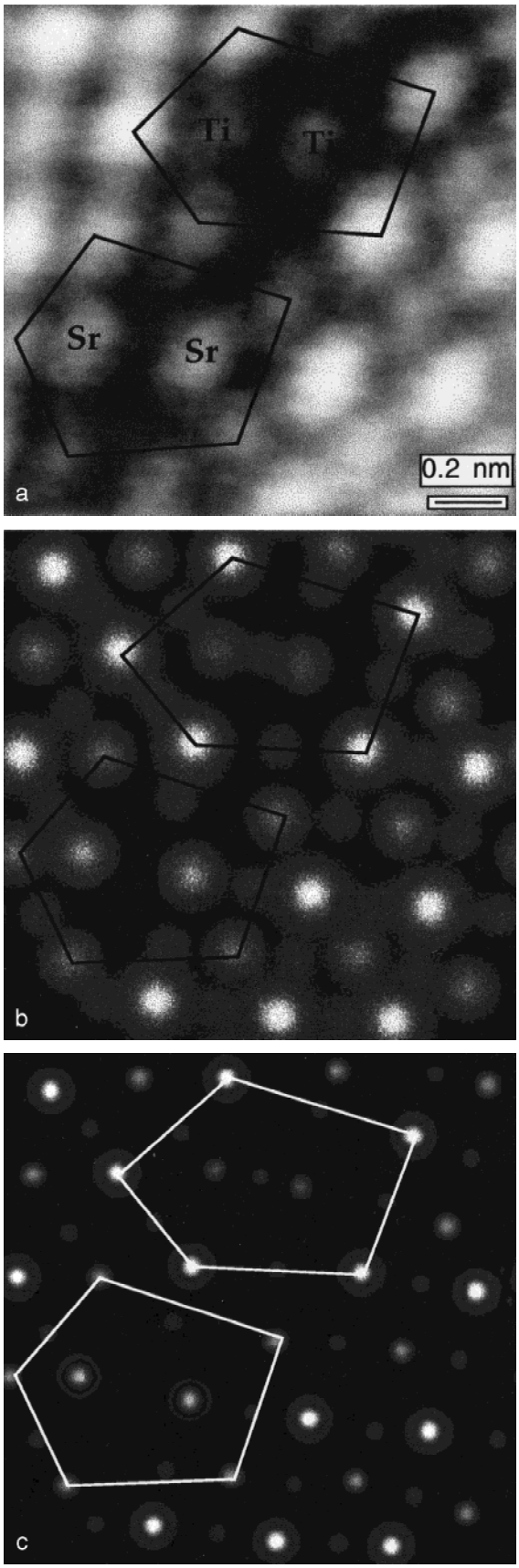

today's probe, and adding random noise to match the experiment. Then the expected noise for the corrected probe can be obtained and added to the simulated image. For comparison, Figure 7c shows the simulated image assuming the free space probe, which shows the distinct subsidiary maxima around each atomic column.

The free space probe will, of course, be appropriate for images of single atoms on the entrance surface of a sample, or very close to it. Figure 8 shows an image of Pt atoms on crystalline γ-alumina obtained with the HB603U (Nellist and Pennycook, 1996), Although the support showed fringes in the bright field STEM image, it was tilted a little off the zone axis and did not show any fringes in Z-contrast. Figure 8b shows a simulated image for the Pt trimer, using positions obtained from first principles density functional relaxations (Sohlberg et al., 1999). The simulation is for zone axis illumination and is obtained by summing simulations for one unit cell of the γ-alumina with the Pt trimer using the free space probe, and adding simulations of a ~5 nm substrate using the effective probe. The Pt atoms are still visible, smaller than the image of the Al and O columns of the support.

Conclusions

The smaller probes available with spherical aberration correction offer dramatic advantages for Z-contrast STEM. With the larger objective apertures, it appears that incoherent imaging conditions will remain with similar annular detector inner angles as today, but the limiting resolution in a zone-axis crystal will become the 1s Bloch states instead of the probe. The Z-contrast image will become a direct image of the 1s Bloch states. Image resolution, contrast, and signal-to-noise ratio will increase significantly, allowing more accurate quantification of atomic positions and intensities. With the greatly enhanced contrast, we anticipate sensitivity to single high-Z impurity atoms in or on a light support, and also light columns such as oxygen close to high-Z columns, as in the $SrTiO_3$ grain boundary. Improved sensitivity will also be seen in EELS. Although the effective probe for the inelastic image is broadened not only by the 1s Bloch

Figure 7. a: Z-contrast image of a 36° $SrTiO_3$ grain boundary showing the reconstructed Ti and Sr dislocation cores that alternate along the boundary plane; **b:** simulated image for the aberration corrected STEM using the effective probe (the free space probe convoluted with a 1s Bloch state); **c:** simulated image using the 0.5 Å free space probe for comparison.

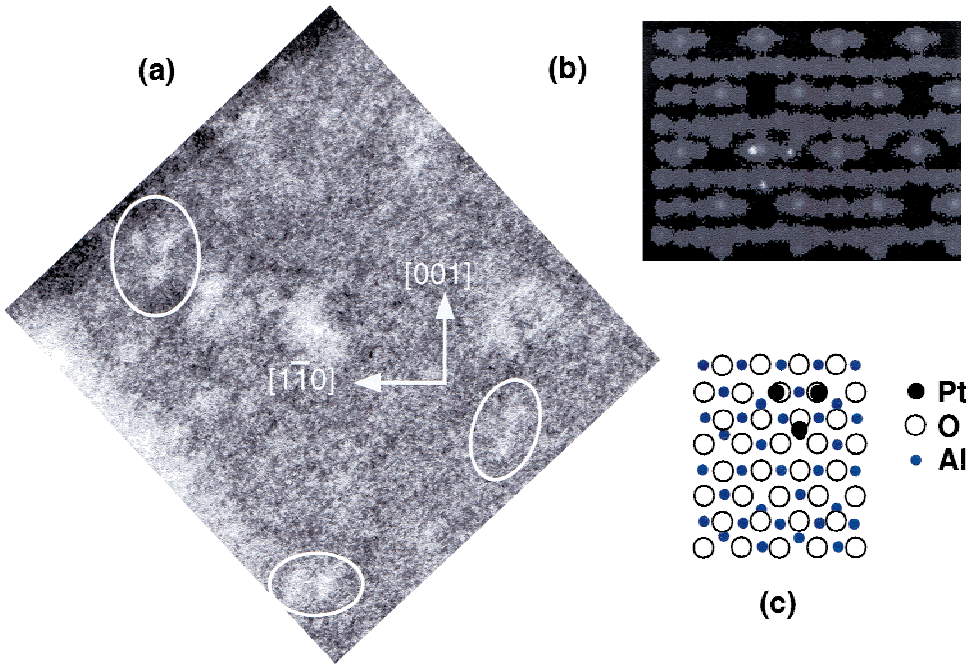

Figure 8. a: Z-contrast image of Pt catalyst atom clusters ultradispersed on a γ-alumina surface; **b:** simulated image of a Pt_3 trimer for the aberration-corrected STEM as described in the text; **c:** relaxed structure projected along [110] showing Pt atoms occupying surface vacancies.

state but also by the width of the inelastic object function, recent calculations suggest that these are intrinsically quite narrow, less than 0.5 Å for core loss excitation above 100 eV (Rafferty and Pennycook, 1999). Therefore, we should see almost as great an improvement in EELS sensitivity; placing the probe over a chosen column, the spectrum will involve excitations almost entirely from atoms within that column, and single impurity atom detection and identification seems likely.

Acknowledgments

The authors are grateful to G. Duscher and V.P. Dravid for the image in Figure 7, and to O. Krivanek for the profiles in Figure 4. This research was supported by Lockheed Martin Energy Research Corp. under DOE contract DE-AC05-96OR22464, and by appointment to the Oak Ridge National Laboratory (ORNL) Postdoctoral Research Associates Program administered jointly by ORNL and the Oak Ridge Institute for Science and Education. P.D.N. acknowledges the Royal Society, London, for support.

References

Anderson SC, Birkeland CR, Anstis GR, Cockayne DJH (1997) An approach to quantitative compositional profiling at near atomic resolution using high-angle annular dark-field imaging. *Ultramicroscopy* 69:83–103

Batson PE (1993) Simultaneous STEM imaging and electron energy-loss spectroscopy with atomic column sensitivity. *Nature* 366:727–728

Browning ND, Chisholm MF, Pennycook SJ (1993) Atomic resolution chemical analysis using a scanning transmission electron microscope. *Nature* 366:143–146

Cherns D, Howie A, Jacobs MH (1987) Characteristic X-ray production in thin crystals. *Z Naturforsch Teil A* 28:565–571

Duscher G, Browning ND, Pennycook SJ (1998) Atom column resolved electron energy loss spectroscopy. *Phys Status Solidi A* 166:327–342

Haider M, Uhlemann S, Schwan E, Rose H, Kabius B, Urban K (1998) Electron microscopy image enhanced. *Nature* 392:768–769

Hall CR, Hirsch PB, Booker GR (1966) Effects of point defects on absorption of high energy electrons passing through crystals. *Philos Mag* 14:979–989

Hartel P, Rose H, Dinges C (1996) Conditions and reasons for incoherent imaging in STEM. *Ultramicroscopy* 63:93–114

Heidenreich RD (1962) Attenuation of fast electrons in crystals and anomalous transmission. *J Appl Phys* 33:2321–2333

Hirsch PB, Howie A, Whelan MJ (1962) On the production of X-rays in thin metal foils. *Philos Mag* 7:2095–2100

Hirsch PB, Howie A, Nicholson RB, Pashley W, Whelan MJ (1965) *Electron Microscopy of Thin Crystals.* London: Butterworths

Howie A (1967) Diffraction channelling of fast electrons and positrons in crystals. *Philos Mag* 14:223–237

Howie A, Whelan NJ (1961) Diffraction contrast of electron microscope images of crystal lattice defects. II: The development of a dynamical theory. *Proc R Soc London Ser A* 263:217–237

Jesson DE, Pennycook SJ (1993) Incoherent imaging of thin specimens using coherently scattered electrons. *Proc R Soc London, Ser A* 441:261–281

Jesson DE, Pennycook SJ (1995) Incoherent imaging of crystals using thermally scattered electrons. *Proc R Soc London, Ser A* 449: 273–293

Krivanek OL, Delby N, Lupini A (1999) Towards sub-Å electron beams. *Ultramicroscopy* 78:1–11

Loane RF, Kirkland EJ, Silcox J (1988) Visibility of single heavy atoms on thin crystalline silicon in simulated annular dark-field STEM images. *Acta Crystallogr Sec A* 44:912–927

Loane RF, Xu P, Silcox J (1992) Incoherent imaging of zone axis crystals with ADF Stem. *Ultramicroscopy* 40:121–138

Mitsuishi K, Kawasaki M, Takeguchi M, Furuya K (1999) Determination of atomic positions in a solid Xe precipitate embedded in an A1 matrix. *Phys Rev Lett* 82:3082–3084

Muller DA, Sorsch T, Moccio S, Baumann FH, Evans-Lutterodt K, Timp G (1999) The electronic structure at the atomic scale of ultrathin gate oxides. *Nature* 399:758–761

Nakamura K, Kakibayashi H, Kanehori K, Tanaka N (1997) Position dependence of the visibility of a single gold atom in HAADF-STEM image simulation. *J Electron Microsc* 1:33–43

Nellist PD, Pennycook SJ (1996) Direct imaging of the atomic configuration of ultra-dispersed catalysts. *Science* 274:413–415

Nellist PD, Pennycook SJ (1998a) Sub-ångstrom resolution TEM through under-focussed incoherent imaging. *Phys Rev Lett* 81: 4156–4159

Nellist PD, Pennycook SJ (1998b) Incoherent imaging using dynamically scattered coherent electrons. *Ultramicroscopy* 78:111–124

Pennycook SJ, Howie A (1980) Study of single electron excitations by electron microscopy. II. Cathodoluminescence image contrast from localized energy transfers. *Philos Mag* 41:809–827

Pennycook SJ, Jesson DE (1990) High-resolution incoherent imaging of crystals. *Phys Rev Lett* 64:938–941

Pennycook SJ, Jesson DE (1991) High-resolution Z-contrast imaging of crystals. *Ultramicroscopy* 37:14–38

Pennycook SJ, Jesson DE (1992) Atomic resolution Z-contrast imaging of interfaces. *Acta Metall Mater* 40:S149–S159

Pennycook SJ, Narayan J (1985) Atom location by axial-electron-channeling analysis. *Phys Rev Lett* 54:1543–1546

Perovic DD, Rossouw CJ, Howie A (1993) Imaging inelastic strains in high-angle annular dark field scanning transmission electron microscopy. *Ultramicroscopy* 52:353–359

Rafferty B, Pennycook SJ (1999) Towards atomic column-by-column spectroscopy. *Ultramicroscopy* 78:141–152

Rayleigh Lord (1896) On the theory of optical images with special reference to the microscope. *Philos Mag* 42:167–195

Scherzer O (1949) The theoretical resolution limit of the electron microscope. *J Appl Phys* 20:20–29

Sinkler W, Marks LD (1999) A simple channelling model for HREM contrast transfer under dynamical conditions. *J Microsc* 194:112–123

Sohlberg K, Pennycook SJ, Pantelides ST (1999) Explanation for the observed dearth of three-coordinated Al on γ-alumina surfaces. *J Am Chem Soc* 121:1099–1101

Spence JCH, Cowley JM (1978) Lattice imaging in STEM. *Optik* 50:129–142

Spence JCH, Tafto J (1983) ALCHEMI: a new technique for locating atoms in small crystals. *J Microsc* 130:147–154

Van Dyck D (1989) The atom column approximation in dynamical electron diffraction calculations. In: *Computer Simulation of Electron Microscope Diffraction and Images,* Krakow W, O'Keefe M (eds). Warrendale, PA: The Minerals, Metals & Materials Society